# Development of the 90-Cell prototype for the SuperNEMO experiment

M. Azmat and A. Walmsley

School of Physics and Astronomy

The University of Manchester

MPhys Project Final Report

May 2009

.

**Abstract**

An investigation into the functioning of drift cells operating in Geiger mode was performed. This was in order to inform the development of the 90-Cell tracker prototype for use in the proposed SuperNEMO experiment. Collected data from January 2009 until May 2009 was analysed to determine the condition of the 90-Cell. Comparisons were made between data that was taken before a period in April 2009 when the tracker was disassembled to be repaired and after it. External pressure and temperature effects relating to the voltage across the tracker was investigated and a system was developed in order to compensate for these.

# Contents

# 1. Introduction

The purpose of this report is to discuss the continued testing of the 90-Cell prototype on which it is hoped that the modules for the proposed SuperNEMO experiment will be based. This prototype is composed of drift cells that are set to operate in Geiger mode and are comparable to those that are used in the current Neutrino Ettore Majorana Observatory 3 (NEMO-3) experiment, which SuperNEMO will supersede.

During its years in operation the NEMO-3 experiment has sought to observe the process of neutrinoless double beta decay ($0\upsilon\beta\beta$) with a view to determine whether the neutrino is of Majorana or Dirac type. Although there have been several experiments with this aim, such as IGEX and COBRA, NEMO-3 is unique in that it is able to measure not only the energies produced in the decay, as do all of the other experiments of this kind, but it is also able to reconstruct the track of any charged particles involved [1]. This is done through the utilisation of the drift cells in Geiger mode. SuperNEMO will use the same principles, but on a larger scale and with greater resolution.

We have been involved in the research and development of the 90-Cell prototype and have previously reported on the initial testing of its electronics and have performed an analysis on the operational efficiency of the Geiger cells. This was performed by powering each individual cell and examining the resultant propagation efficiencies. We have also discussed the development of the data analysis software that was used to examine simulated data. Since the completion of this earlier report the Geiger cards that are used to readout all 90 cells at the same time were installed, which allowed the prototype to function as a complete tracking chamber. This also allowed for the collection of real data, the analysis of which is to be the primary subject of this report.

Shortly after the tracker became fully operational it was also found that the effective voltage at which the Geiger cells were operating was being affected by variations in atmospheric pressure and the surrounding temperature. Therefore we sought to investigate this relationship with the ultimate aim being to correct for the expected effect of pressure and temperature by automatically adjusting the input voltage.

### 1.1 Double Beta Decay

Within recent years, it has come to be established, through experiments such as KamLAND and SNO [2], that neutrinos have non-zero mass. This has been determined to be of the order of $10^{-6}$ of the mass of the electron. Despite it being exceedingly small having a mass allows the concept of neutrino oscillations. There are some properties of neutrinos that are still to be investigated.

This is the primary motivation of the study of neutrinoless double beta decay ($0\upsilon\beta\beta$). The comparable process allowed by the Standard Model is double beta decay ($2\upsilon\beta\beta$), as shown in Figure 1.1(a), it is possible to draw some conclusions about the properties of the neutrino type. $2\upsilon\beta\beta$ decay has a lifetime of the order $10^{20}$ years and occurs when two neutrons decay and is described by the following process:

$$2n \rightarrow 2p + 2e^{-} + 2\overline{\nu}_{e} \,, \qquad (1)$$

In the above process charge, spin and lepton number are conserved and the neutrino would be of Dirac type.

The process of $0\upsilon\beta\beta$, as shown in Figure 1.1(b) can be represented as:

$$2n \rightarrow 2p + 2e^{-}, \tag{2}$$

which would involve the exchange of the Majorana neutrino in the decay process. It is important to note that this violates lepton number since electrons are produced after the decay, which each have a lepton number of one. Unlike $2\upsilon\beta\beta$ there is no antineutrino to balance this therefore in order for this process to occur the Majorana neutrino would have mass and be its own anti-particle. This process is yet to be observed although claims are being disputed over its existence [3].

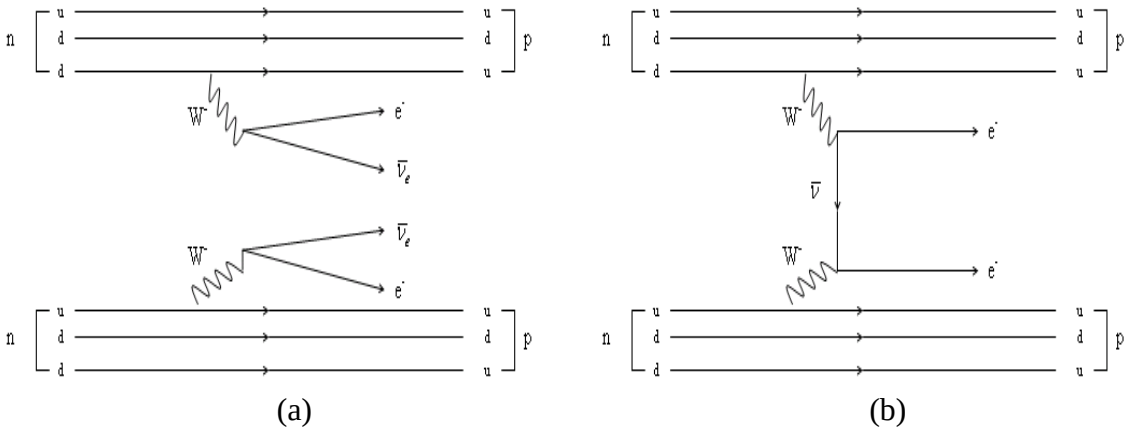


*Figure 1.1: Feynman diagram of the two possible double beta decay processes (a) double beta decay (b) neutrinoless double beta decay*

Nuclear double beta decay occurs only in even-even nuclei. These are bound more tightly than odd-even or odd-odd nuclei due to the pairing energy as given by the semi-empirical mass formula (SEMF). In these nuclei single beta decay can be either strongly suppressed or even energetically forbidden. This reduces the background to allow for the study of $2\upsilon\beta\beta$. This could result in the transition to the next even-even nucleus via the process:

$$(A, Z) \rightarrow (A, Z+2) + 2e^{-} + 2\bar{\nu}_e, \tag{3}$$

where $A$ is the nucleon number and $Z$ is the atomic number or charge of the nucleus.

This process is highly improbable since it requires the simultaneous decay of two neutrons and has a lifetime of the order $10^{20}$ years although it has been observed. The first observation was in 1950 by Inghram and Reynolds [4]. The half-life, $T_{1/2}^{2\nu}$ of the process can be calculated from:

$$(T_{1/2}^{2\nu})^{-1} = \left|M_{2\nu}\right|^2 \times G^{2\nu}(Z,Q), \tag{4}$$

where $M_{2\nu}$ is the nuclear matrix element (NME) and $G^{2\nu}$ is the phase space factor for the process, which is a function of its charge and Q-value and can be calculated exactly.

For $0\upsilon\beta\beta$ in nuclei, the proposed transition is:

$$(A,Z) \rightarrow (A,Z+2) + 2e^{-}. \tag{5}$$

The half-life of the process is given by:

$$(T_{1/2}^{0\nu})^{-1} = \left|M_{0\nu}\right| \times G^{0\nu}(Z,Q) \times \left\langle m_{\beta\beta} \right\rangle^2, \tag{6}$$

where $M_{0\nu}$ is the nuclear matrix element (NME), $G^{0\nu}$ is the phase space factor for the process and $\left\langle m_{\beta\beta} \right\rangle$ is the effective neutrino mass. This is defined as:

$$\left\langle m_{\beta\beta} \right\rangle = \sum_{i=1}^{3} m_i U_{ei}^2, \tag{7}$$

where $m_i$ is the mass of neutrino type $i$ and $U_{ei}$ is the neutrino mixing matrix.

During this process there are several stages. In the first decay an electron and a virtual anti-neutrino are emitted followed by a second decay where a second electron is produced. For this to occur a virtual neutrino must be absorbed and therefore this virtual neutrino must be identical to the anti-neutrino. Because of this it is necessary that the Majorana particle is its own anti-particle. The neutrino emitted in the first decay will have right-hand helicity due to the parity violation in the weak decay and the electron has left-hand helicity. This suggests that due to angular momentum conservation the second electron will be left-handed and the helicity of the neutrino will be reversed.

There are two ways to provide this reversal of helicity. The first is a result of the existence of a W-boson that is massive, i.e. greater than 100 GeV. It will also have a right-handed helicity in weak interaction, which will give particles an equivalent helicity. The second way is due to the non-zero rest mass of the neutrino. The helicity is then reversed due to having a coordinate system that travels faster than the neutrino since it cannot travel at the speed of light. The most reasonable explanation for the existence of a neutrino rest mass is a consequence of the violation of lepton number conservation. This suggests that the known mechanisms for giving a neutrino a mass require that it is a Majorana neutrino [5].

Since the neutrinos cannot be directly detected it is not possible to distinguish between neutrino type therefore it is necessary to examine the energy spectrum of the emitted electrons in order to infer the properties of the neutrino. Double beta decay will produce a continuous distribution since the energy is shared between the electrons and neutrinos. Neutrinoless double beta decay will, however, produce a single sharp peak that would be observed near the Q value at the end of a double beta decay spectrum. This is shown in Figure 1.2, although it should be noted that the $0\upsilon\beta\beta$ peak on the diagram is exaggerated and a real signal be seen as a slight alteration to the tail of the distribution

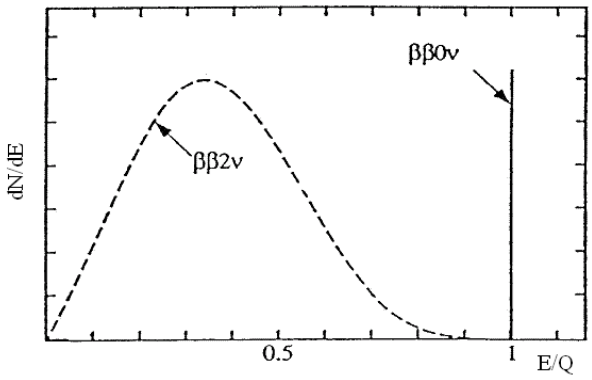


*Figure 1.2: Theoretical energy spectrum of double beta decay electrons produced in 2νββ and 0νββ decay*

## 1.2 The SuperNEMO Experiment

SuperNEMO will use a tracking and calorimetry approach as used in NEMO-3. The detector will consist of twenty individual modules. Each module will consist of over two thousand wire drift chambers and one thousand scintillator blocks and will each hold 5 kg of isotope giving the construction a very high mass sensitivity of about 50meV. Of the available even-even nuclei one or two isotopes will be used that have the optimum characteristics for $0\upsilon\beta\beta$ to be observed. The tracking volumes will surround the source foil, as shown in Figure 1.3.

The scintillators will be arranged into large blocks that make up the calorimeter and will be read out by photomultiplier tubes (PMTs). They will be able to measure the time of flight of the particles, which is needed to reconstruct the position of the particle in three dimensions. This information is partly needed in order to reject crossing electrons that are produced in the decay process. There will also be a magnetic field of 25 G parallel to the plane of the source foil in order to distinguish between electrons and positrons [6].

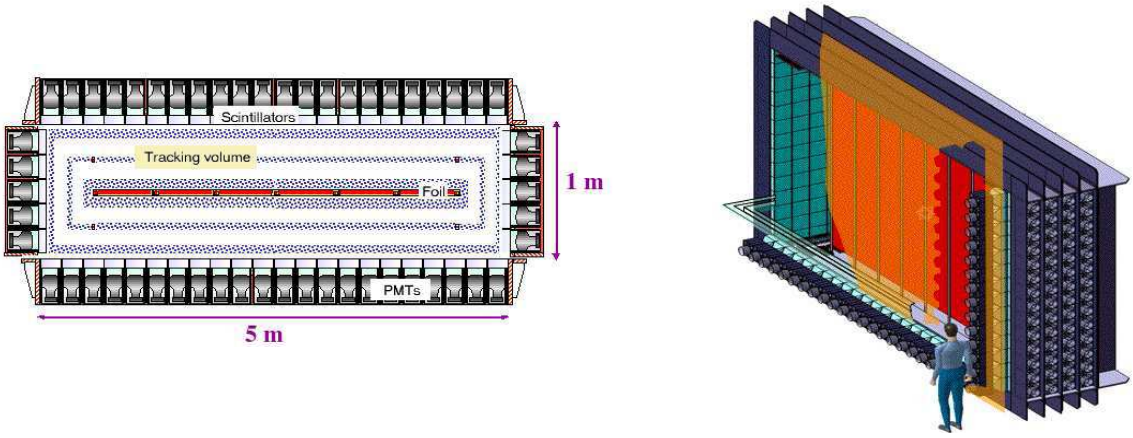


*Figure 1.3: The proposed construction of a SuperNEMO module*

# 2. The Physics of Geiger Cell

## 2.1 Geiger Cells

SuperNEMO, like its predecessor NEMO-3, utilises drift cells operating in Geiger mode in order to reconstruct a three dimensional track of an incident charged particle. Each cell consists of an anode wire surrounded by eight ground wires with copper cathode rings at each end. Figure 2.1 is a schematic diagram of a Geiger cell used in NEMO-3. It is similar in construction to that of a SuperNEMO, but with different dimensions, which are 350 cm in length with a diameter of 4.4 cm. The wires are required to be at relatively high tension to ensure good plasma propagation.

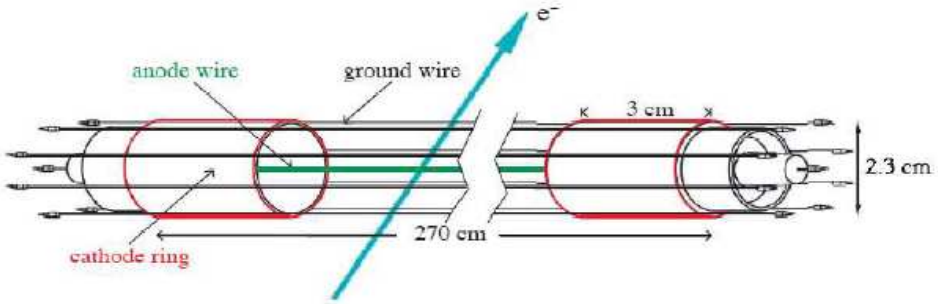


*Figure 2.1: A simple Geiger cell as used in NEMO-3*

The cells are placed in a gas mixture of helium and ethanol. Charged particles that travel through the cell ionise a small number of helium molecules and the free electrons create an avalanche process, which ultimately creates a pulse on the anode wire. Using a network of Geiger cells an incident particle's track can be reconstructed. (corrected this now we have better understanding of tracking)

## 2.2 The Avalanche Process

An incident particle entering the active volume of a Geiger cell will ionise a small number of helium atoms within its volume. The free electrons produced drift towards the anode wire due to its electric field. The field accelerates the electrons so much so that they gain enough energy to ionise further helium atoms and this produces more electrons. This process continues and increasing numbers of electrons are produced creating an avalanche of electrons drifting towards the anode wire. This is shown in Figure 2.2(a) and 2.2(b), where the drift time, $t_{d,}$ is the time taken for a cascade of electrons to reach the anode wire from the initial ionisation point.

During an avalanche several UV photons are emitted by excited nuclei returning to the ground state. The majority of these photons are short range and have enough energy to ionise further gas molecules. This initiates further avalanches in the local area. The avalanches created result in increasing densities of helium ions near to the anode wire. This reduces the electric field in the local vicinity. Due to this ionised electrons will gain less and less energy. This continues until the ions cancel enough of the electric field that electrons do not have the sufficient energy to ionise helium. As a result of this no more UV photons are emitted. The avalanche process in the vicinity then dies out and the local area becomes a "burnt out" region, shown in Figure 2.2(c), resulting in the relatively long dead time of 1ms. It is the time it takes for the ions to drift away to a cathode returning the electric field to its normal level.

Photons that escape the vicinity instigate further avalanches and the whole process repeats creating plasma propagation along the wire, adding charge to the anode wire as it propagates. When plasma reaches the cathode rings it produces an output signal which is used in the tracking of the incident particle. This is shown in Figure 2.2(d) and discussed in further detail in section 3.3. At higher voltages all the aspects of the avalanche mechanism occur more smoothly and quickly. As such blockages and defects on the wire can be passed more easily (see section 2.7). For a more in depth analyses of plasma propagation consult Wilkinson (1992) [7].

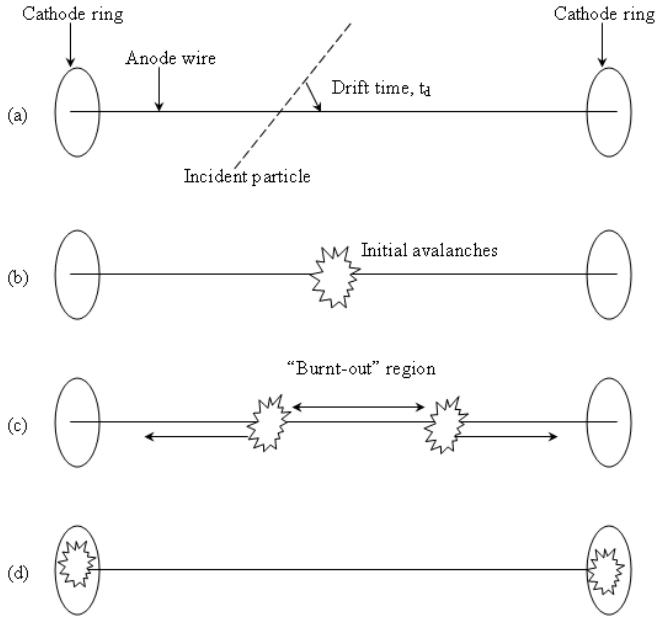


*Figure 2.2: The sequence of events in the plasma propagation process*

## 2.3 The Gas Medium

The gas medium consists of a mixture of helium (96%) and ethanol (4%). Helium, due to its low mass, is ideal for minimising the energy incident charged particles lose upon collision therefore it is the dominant fill gas. A small amount of ethanol is also introduced to act as a quenching gas.

## 2.4 The Quenching Gas

When a helium ion comes into contact with a cathode it is neutralised and placed in an excited state. It then emits a photon and becomes de-excited. There is the possibility, if the photon is of sufficiently high energy, that it will liberate an electron from the cathode material. This electron can then create a further avalanche and thus create more ions. This process is more pronounced with higher voltages eventually leading to the onset of continuous discharge. This is where the increased voltage causes the process to continually repeat itself resulting in the repeated firing of the cathode.

This can be prevented via internal or external quenching. External quenching involves decreasing the high voltage on the anode immediately following the first avalanche. The disadvantage of this is an increase in the dead time of the cell since the voltage can only be increased back to normal once all ions have been neutralised.

In NEMO-3 internal quenching was preferred, which is the case for SuperNEMO. This involves adding a small amount of compound to the gas mixture in order to absorb excess UV photons. A good quenching gas has to have two main properties:

- A lower ionisation potential than the fill gas, which is helium.
- The ability to photo-decompose. This is the tendency for a molecule to break apart when it absorbs a photon.

Ethanol has both of these properties. The lower ionisation potential than helium causes ethanol ions to interact with helium ions and exchange an electron. Therefore closer to the cathode there are increasing numbers of ethanol ions and fewer helium ions. The ethanol ions are neutralised at the cathode before decomposing. This reduces the possibility of continuous discharge until very high voltages are reached.

Ethanol was chosen for NEMO-3 because in addition to the above properties it has many vibrational and rotational energy levels. This gives it a wide spectrum for absorbing UV photons. Upon absorption the ethanol then photo-decomposes.

An unfortunate consequence of using a quenching gas is that its decomposition products can be deposited on the anode wire. This, in the long term, produces an aging effect as the polymers on the anode could build up and prevent plasma propagating past [8].

### 2.5 Geiger Mode

Geiger mode requires a high voltage to be applied on the anode wire. At these voltages the amount of electrons produced by a charged particle ionising the gas medium is independent of its energy. Instead it depends on the voltage along the cell. Anode pulses produced are typically in the order of 100 mV. This relatively large signal allows readout using a simple RC circuit. Another advantage of the large pulse produced on the anode wire is that it allows for plasma to propagate to the cathode rings, which results in a three dimensional construction of a charged particle's path through the tracker. This is done by measuring the time taken for each pulse to reach a cathode ring at either end of the anode wire. The large output signal is the principle advantage of Geiger mode over proportional mode.

In Geiger mode a cell has a relatively long dead time of 1ms due to the electric field needing to recover to its original state after an avalanche occurs. This makes it unsuitable for experiments with high event rates. However, SuperNEMO, in its final state, will have an event rate of ~100Hz, which is suitable.

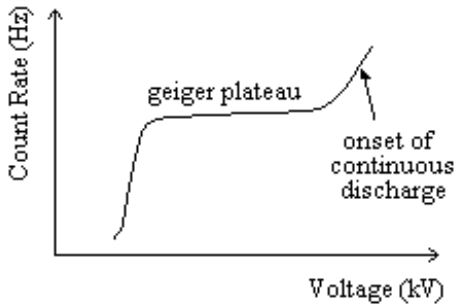


*Figure 2.3: The theoretical plot for count rate against voltage for a Geiger cell*

The theoretical behaviour of a drift cell at different voltages when making the transition from proportional mode to Geiger mode is shown in Figure 2.3. Event rates are initially low as it makes the transition from proportional mode to Geiger mode. The mode of operation is on the Geiger plateau. At higher voltages the cell enters continuous discharge.

## 2.6 Typical Readout

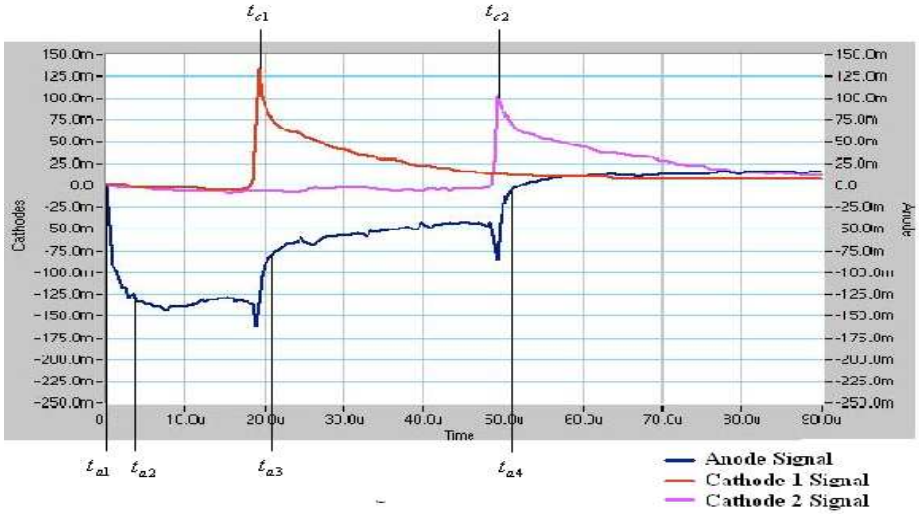


*Figure 2.4: Typical Geiger cell event*

Figure 2.4 show the readout for a typical Geiger cell event where $t_{a1}$ is the time at which the initial avalanche of electrons reaches the anode wire. At $t_{a2}$ the plasma has begun to propagate in both directions from the point of the initial avalanche. This adds charge at a relatively constant rate. The slight gradient is due to the RC circuit readout.

At $t_{a3}$ plasma in one direction has propagated to the end of the wire. With plasma now only propagating in one direction, charge is added to the wire at half the initial rate. At $t_{a4}$ the remaining plasma has reached the other end of the wire. No more charge is added to the wire therefore the voltage returns to its base level.

Considering the cathode signals, when plasma reaches the cathode rings the sudden increase in electric field strength attracts ions to the copper cathode rings upon which they recombine with an electron. This process accounts for the spike of charge seen at $t_{c1}$ and $t_{c2}$. It is also important to note $t_{c1} \approx t_{a3}$ and $t_{c2} \approx t_{a4}$. Propagation time, $t_p$, is defined as the amount of time it takes plasma to propagate from one end of a Geiger cell to the other and is given by:

$$t_p = (t_{a3} - t_{a2}) + (t_{a4} - t_{a2}). \qquad (8)$$

The pulse height of the anode, i.e. the amplitude difference between $t_{a1}$ and $t_{a2,}$ defines the amount of charge added to the anode by the initial plasma propagating in both directions. It will increase with anode voltage due to an increased electric field giving incident electrons more energy.

Propagation efficiency is defined as the ratio of events in which plasma successfully propagates to both cathode rings to the total amount of events. This provides an important measurement of cathode efficiency.

## 2.7 The Nature of Blockages

Blockages on the anode wire can arise for various reasons. Firstly, substances can be deposited on the anode wire during Geiger cell production or installation, a human hair for example. This can prevent plasma from propagating past it. In addition when the detector is operating the products formed from the breakdown of quenching gas molecules can be deposited on the anode wire eventually resulting in a blockage [8]. Before an arrangement of Geiger cells are placed in an isolation chamber they are sprayed with nitrogen to remove any possible blockages. However, this cannot guarantee the removal of all blockages.

There are various forms of blockages that can occur based on the level of impairment they have on a cells performance:

- Partial blockages result in a decrease in probability of successful plasma propagation past them. On some occasions plasma will still propagate past. The chance of success increases with increasing voltage.

- Full blockages heavily decrease the probability of successful plasma propagation even at high voltages. The blockage is simply too substantial for UV photons to overcome, initiating avalanches on the other side on a regular basis.

There is also the possibility of more than one blockage on a wire. There are means to calculate where a blockage is situated on a wire in order to remove it when the cell can be removed from its isolation chamber as shown in section 4.4.

## 2.8 Pressure and Temperature Effects

In order to achieve constant total propagation time of the cells it is necessary to maintain a constant voltage across them. As discussed there are many factors that affect the effective voltage, such as the composition of the gas. Through examination of the propagation time of cell 90 it became apparent that the voltage was also being affected by atmospheric pressure and the temperature of the surroundings. The pressure in particular can change quickly over relatively short periods of time (since the tracker is in a room that has a relatively constant temperature). By measuring the temperature, $T$, and pressure, $P$, it is possible to scale the applied voltage, $V_a$, in order to determine the effective voltage, $V_{eff}$, of the cells as given by the relationship:

$$V_{eff} = V_a \frac{P_0}{P} \frac{T}{T_0}, \tag{9}$$

where $P_0$ and $T_0$ are standard pressure and temperature respectively [9].

This relationship is determined by firstly considering that the electric field strength, $E_s$, within the cells is given by the product of the applied voltage and the geometry of the cells. The energy that the individual electrons gain through collisions is given by:

$$E = E_s d , \tag{10}$$

where *d* is the distance between the atoms. This distance is inversely proportional to the density of the gas and therefore the ratio of temperature and pressure as given by the Ideal Gas equation.
The effective potential is also proportional to the energy gained by the atoms through collision as shown in equation (9). By logging the pressure and temperature at regular intervals it would be possible to write software that can automatically adjust the applied voltage to compensate for the shifts in pressure and temperature. This would allow a relatively constant effective voltage to be maintained across the entire tracker.

# 3. 90-Cell Prototype

The 90-Cell prototype is the current phase in the tracker development for SuperNEMO. It consists of 90 Geiger cells arranged in nine layers each containing ten cells with no offset in cell position between the layers. Geiger cards are used to readout all ninety cells. The numerical increase in cell numbers over the 9-Cell prototype, which preceded it, allows much more accurate tracking of an incident charged particle [10].

## 3.1 Current Status

Prior to March 2009, the 90 cells were analysed by powering cells individually to investigate their propagation efficiency, which was found to be poor in twenty-two cells and is detailed in Figure 3.1. Using timing information allowed the location of these blockages along the anode wire to be found. Other problems included cells 68 and 78, which were found to be unresponsive due to a broken wire shorting them. Also cells 43 and 73 observed too many events suggesting the occurrence continuous discharge. The cell map shown in Figure 3.2(a) details these issues.

| | Blockage position | | |
|---|---|---|---|
| Cell Number | Before opening | After opening | Efficiency after |
| 12 | partial 32 cm from C1, full 105 cm from C2 | partial 32 cm from C2 | 71.10% |
| 15 | partial 24 cm from C2 | partial 26 cm from C2 | 76.20% |
| 18 | patial 105 cm from C1 | Working | |
| 24 | full 23 cm from C2 | Working | |
| 27 | Working | partial 162 cm from C2 | 76.37% |
| 28 | partial 79 cm from C1 | partial 79 cm from C1 | 78.81% |
| 29 | full 145 cm from C2 | Working | |
| 30 | partial 124 cm from C1, full 69 cm from C2 | Working | |
| 33 | partial 56 cm from C1 | Working | |
| 35 | full 10 cm from C2 | full 6 cm from C2 | 2.60% |
| 36 | full 61 cm from C2 | Working | |
| 38 | full 67 cm from C2 | Working | |
| 39 | full 80 cm from C2 | Working | |
| 40 | full 80 cm from C2 | Working | |
| 42 | full 94 cm from C2 | partial 89 cm from C2 | 20.56% |
| 43 | partial 102 cm from C1 | partial 103 cm from C1 | 85.67% |
| 45 | full 124 cm from C2 | full 125 cm from C2 | 1.85% |
| 55 | partial 31 cm from C2 | partial 34 cm from C2 | 59.20% |
| 63 | full 49 cm from C2 | Working | |
| 72 | partial 80 cm from C1 | C1 inefficient | 85.70% |
| 80 | partial 83 cm from C1 | partial 84 cm from C1 | 53.10% |
| 81 | Working | full 112 cm from C1 | 2.10% |
| 96 | Working | C2 inefficient, small signals | 71.80% |
| 97 | not localised | Working | |
| 99 | partial 71 cm from C1, 85 cm from C1 | partial 172 cm from C1 | 83.10% |

*Figure 3.1: Location of blockages with in the 90-Cell before and after disassembly*

All 90 Geiger cards were installed into the tracker readout in early March 2009, full data runs encompassing the whole tracker were then taken and tracking was implemented. Following this during a period in April the 90-Cell was disassembled to inspect the operation of cells showing poor propagation efficiencies. Since cells 68 and 78 were known to have shorted wires they were repaired. Upon inspection some wires where found to have physical blockages, but no blockages were observed on others. A possible explanation for this may that there were defects on the anode wire. These would prevent the successful propagation of the plasma in a similar manner to that of a physical blockage.

After the tracker was reassembled and the gas mixture was reintroduced data was taken to analyse the cell chamber in its new state. Many blockages had been removed but a few new blockages were found on various cells that were not there previously as shown in Figure 3.1. These may have come about due to the cleaning and reassembly procedure. A cell map of the 90-Cell condition following the disassembly can be seen in Figure 3.2(b).

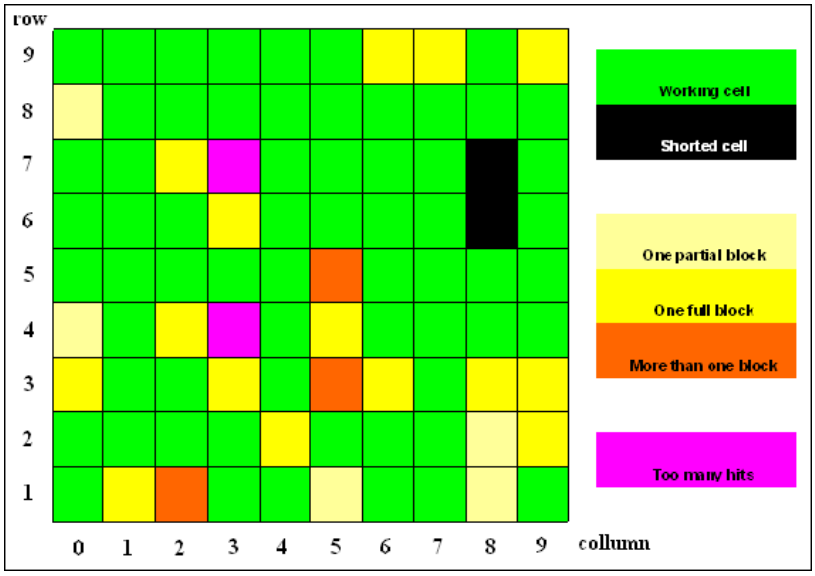


(a)

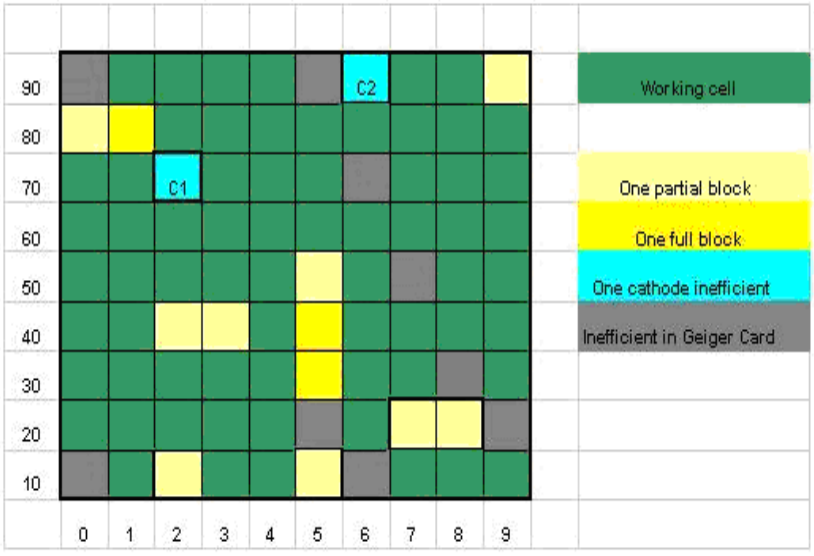


(b)

*Figure 3.2: 90-Cell map (a) before and (b) after Geiger card installation and disassembly for cleaning*

Upon observing data it became apparent that certain cells appeared to be inefficient due to the Geiger card readout. Some cards have problems making them inefficient in recording cathode times as discussed in section 4.

### 3.2 90-Cell Timing

The data that was analysed currently uses two scintillators as triggers. These were placed above and below the 90-Cell. When an incident particle passes through both scintillators a narrow pulse is produced. Their coincident signal initiates the timing of the event. Timing of events is highlighted in Figure 3.3.

Considering a single cell, when an incident particle enters its tracking volume the avalanche produced gives an anode pulse, as shown in Figure 2.4. This initialises timing of three time to digital converters (TDC) in the cell's Geiger card. $TDC_A$ is used to derive the anode drift time, $t_d$:

$$t_d = T_{DELAY} - TDC_A, \tag{11}$$

where $T_{DELAY}$, is the time of a scintillator pulse that is delayed by a set arbitrary amount.

$TDC_{C1}$ and $TDC_{C2}$ record the times of the cathode 1 and cathode 2 pulses respectively. On reaching the cathode rings the pulses are amplified in the Geiger card and then tested against a set threshold voltage. If the pulse height is above the threshold it is accepted and the Geiger card records the time of the pulse. If the signal does not pass the threshold due to a blockage, for example, the timing continues until an upper limit. By making cuts below this upper limit we were able to study the detection efficiency of cathode pulses as discussed in section 4.2.

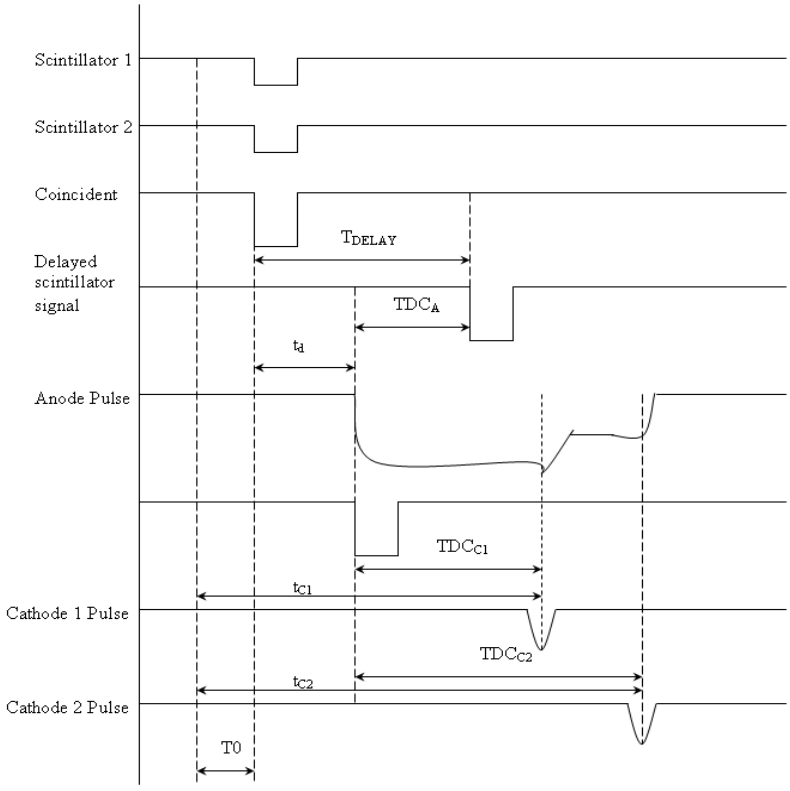


*Figure 3.3: Timing of a event in the Geiger card readout*

### 3.3 The 90-Cell Tracking Programmes

The tracking programme uses the output from the Geiger cards to reconstruct the track of an incident particle through the 90-Cell tracker [11] [12], as shown in Figure 3.4.

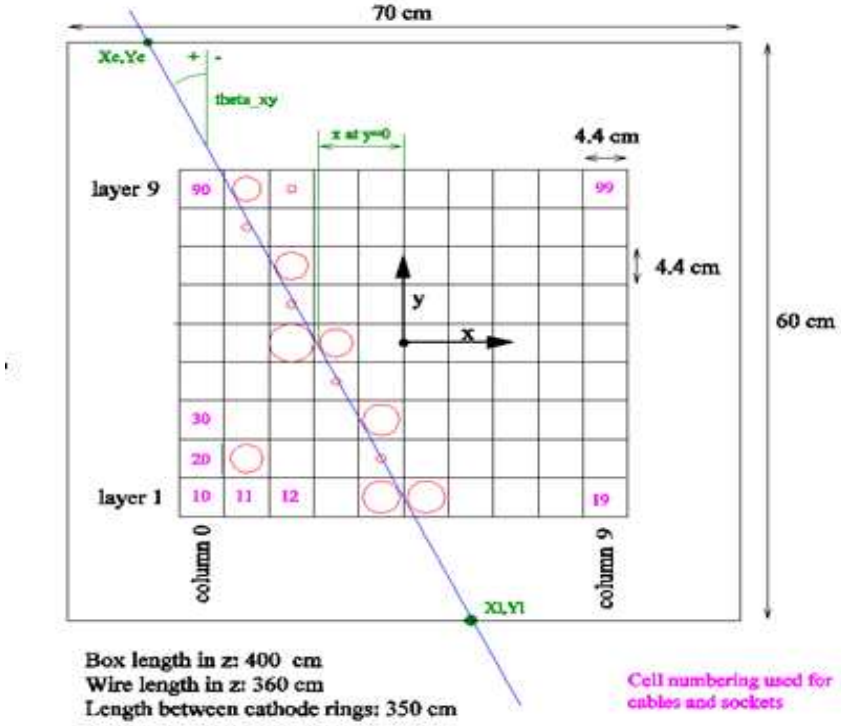


*Figure 3.4: Fit of incident particle through the tracker in the ZY-plane [11]*

A typical tracked event is triggered with an incident particle passing through the two scintillators. As it passes through the active volume of each Geiger cell an avalanche process occurs and anode drift time, $T_A$, is recorded and the cell is said to be "hit". $T_A$ is defined as:

$$T_A = t_d + T0, \tag{12}$$

where $t_d$ is the time taken for an electron cascade to reach the anode wire from the initial ionisation point, as shown in Figure 3.3 and *T0* is difference in time between the trigger initiating and $t_d$ starting. This takes into account electronic delays.

Following this is pattern recognition where the tracking programme attempts to connect hit cells. It attempts to connect cells on the same layers first. If no adjacent hit cells exist on the same layer it looks at adjacent layers. It then connects all cells ±2 layers from each other. This allows for cell inefficiencies. It ensures that in good events all connections are made successfully even if a layer exists that has no hit cells. Z-position information for hit cells utilises cathode times [12]. If one cathode time is missing due to cell inefficiency the Z-position can be reconstructed using the remaining cathode time $T_C$:

$$Z = T_C v_p, \tag{13}$$

where $v_p$ is the velocity of propagation down the anode wire. Following this unwanted hit cells are removed from the event. Based on the tracker volume connections between cells are

removed if their length is greater than 124 mm. This discounts cells triggered by noise. Cellular automation then calculates the probable path of the incident particle through the tracker using the remaining connected cells. These cells are marked as “good hits”. The tracking programme favours a long path containing the greatest amount of good hits as shown in Figure 3.4.

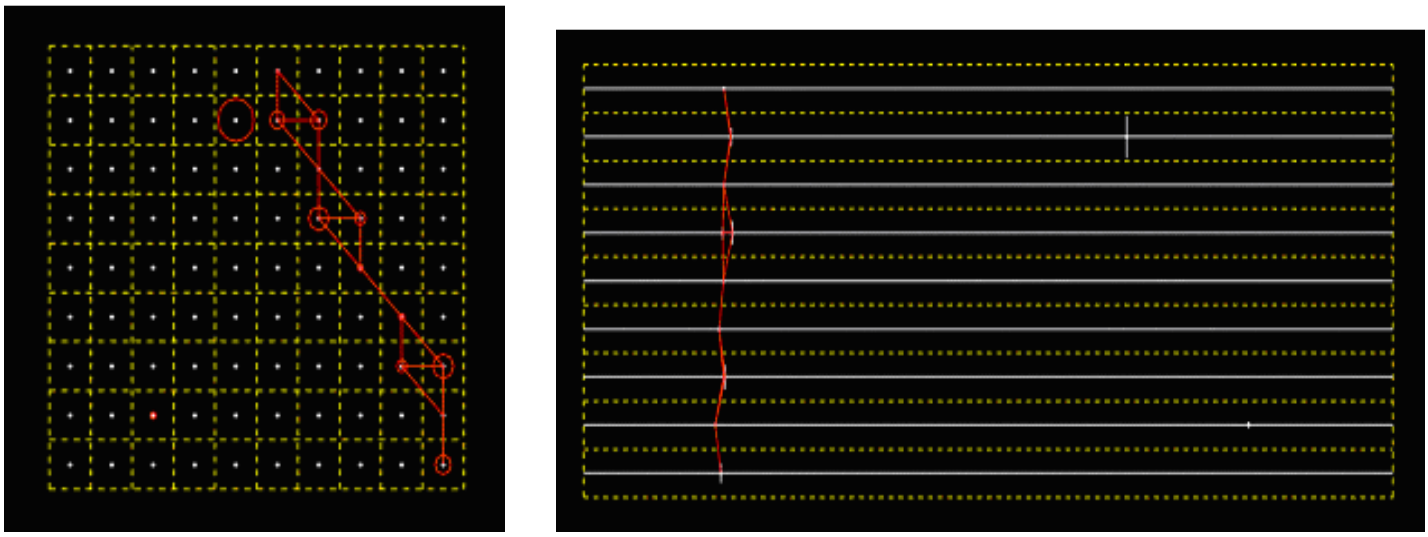

(a) (b)

*Figure 3.5: Track fit (a) in XY Plane, displaying tracking programme connecting hit cells (b) in ZY plane [12]*

The initial track fit is a straight line fit using the coordinates of the central anode wires in all cells recording a good hit as its basis. The conditions for this are that an event must have at least six good hits. Next the tracking programme compares $t_d$ for all good hits. The minimum value, $t_{d\,\min}$, is then subtracted from $T_A$ of all cells, as defined in equation (12), leaving:

$$T_A = t_d + T0 - t_{d\,\min}\,. \tag{14}$$

The tracking programme then varies the gradient, x intercept and $T0$ of the fit until a minimum $\chi^2$ is achieved. This is done because the left/right ambiguities of hits means an exact solution cannot be found. The values of intercept and gradient are recorded in a 2-dimensional array.

# 4. Data Analysis Using ROOT

Data from the tracking programme was analysed using ROOT [13]. The code used compiled all events storing useful parameters in various arrays. This report uses data taken up until April 2009. Data was compared to observe the changes made to the 90-Cell when it was inspected in mid-April. This is discussed in section 5.2.

It should be noted that all the real data samples included in the analysis required all events to have a track fit. The tracker was found to record events in which large quantities of cells fire due to noise. As these events were unphysical they were cut from the analysis.

The Geiger cards used threshold voltages to distinguish real cathode pulses from small pulses generated by noise triggered cells. The threshold values are in hexadecimal format. The range 60 to A0 was determined as in the applicable voltage range for the pulses. Data was collected over various thresholds to study the effects on the tracker. At low thresholds a greater proportion of cathode pulses from real events are accepted. However cells triggered by noise are more likely to be accepted. The T60 threshold data was chosen to be included in this report because cathode pulses in real events will be accepted most often and the tracking programme will always eliminate the vast majority of noise triggered cells in real events. For comparison of the thresholds see section 4.6.

Effective voltage was also altered in various data sets. As explained this changes the electric field strength and thus the size of the pulses involved. Of the data shown (unless otherwise mentioned) the cells are powered at 1550V.

Finally, the data sets are all triggered using two scintillators. As a consequence there are various features of the data shown that can be attributed to the position of the scintillators relative to the detector.

## 4.1 Cathode Times

To look at cathode efficiency we investigated cathode 1 and 2 times. Figure 4.1 displays the mean cathode 1 times recorded for data taken at threshold T60. The majority of cells recorded cathode 1 and 2 times around 50 µs and 20 µs respectively. The scintillators did not cover the entire length of the tracker, but were positioned closer to cathode 2.

.

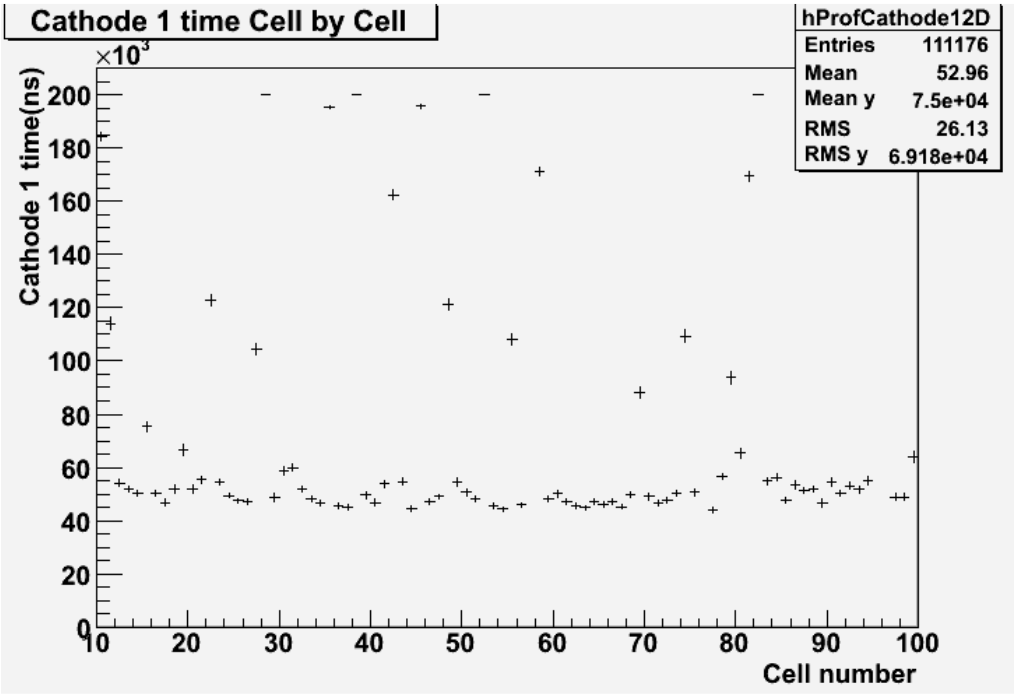


*Figure 4.1: Cathode 1 times of all 90 cells for threshold T60 data*

Cathode inefficiencies were due to blockages, possible wire defects in the tracker and inefficient Geiger cards. Cells that do not record a cathode hit within the upper limit of the Geiger card are assigned the arbitrary cathode time of 200µs. As can be seen from figure 4.1 cells 28, 38, 45, 52, 95 and 96 recorded a mean close to or exactly 200 µs suggesting zero cathode efficiency. This implied that in these cells there was either a full blockage between the scintillator position and cathode 1 or the Geiger Card was not functioning correctly. Cathode 2 information suggests that cells 20, 28 and 38 were completely inefficient in the cathode. By cross checking this with blockage information, shown in Figure 3.1, it was concluded that of the mentioned cells cell 20 was inefficient in cathode 1, cells 52, 95 and 96 were inefficient in cathode 2 and cells 28 and 38 were inefficient in both cathodes. This was assumed to be related to the Geiger card readout.

Cells with cathode times in the range 60 µs and 200 µs had partial blockages or Geiger card readout inefficiencies. It was also noted that cells 57 and 76 recorded nothing for the cathode times suggesting the TDCs on the Geiger cards for these cells were not working correctly.

It was made aware that during the late period in April some Geiger cards had been modified in order to improve the functionality of all of the cards. This could explain why there are

discrepancies between these results and those that are shown in Figure 3.2(b), which was created using data that was taken before this period.

### 4.2 Detection Probability

Figure 4.2 shows the detection probability, $D_P$, at threshold T60, for all 90 cells. It is the probability of both cathodes signals being registered in a cell after plasma propagation has occurred. When the Geiger card upper timing limit is reached and a cathode hit has not been registered an arbitrary value of 200 µs is recorded. Denoting these unregistered hits in a cell as $N_{UH}$, $D_P$ can be defined as:

$$D_P = \frac{N_T - N_{UH}}{N_T}, \tag{15}$$

where $N_T$ is defined as the total amount of hits for a given cell. It should be noted that this is not propagation efficiency due to readout issues also being factored into cathode efficiencies.

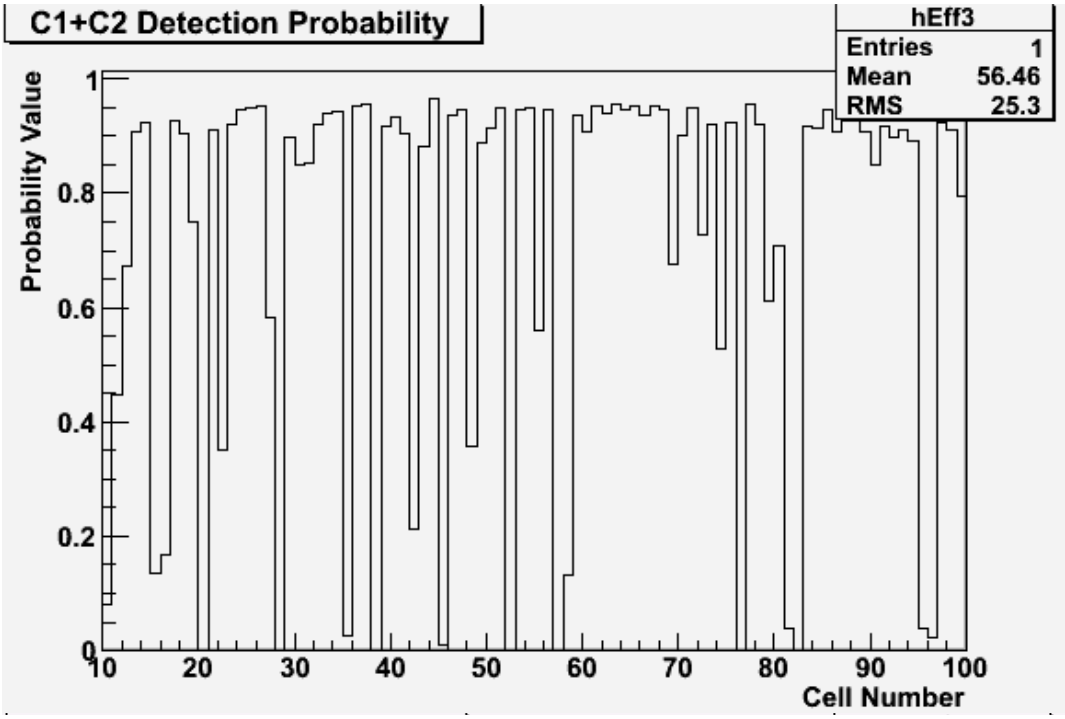


*Figure 4.2: Detection probability of both cathode times at threshold T60*

In Figure 4.2 cells showing poor detection probabilities are those that are mentioned in section 4.1 whilst cells with partial blockages or partially inefficient Geiger card timings have $D_E$ ranging from 0.1 to 0.8. When all 90 cells and their Geiger cards are functioning correctly each one should have a detection probability of approximately 0.97 at threshold T60.

### 4.3 Gradient Distribution

Figure 4.3 shows the values of gradient from the tracking programme fit. This is the gradient of the reconstructed track in the XY-plane with respect to the x axis. The scintillators are laid out across the top and bottom of the detector, but they do not overhang it excessively. An incident particle entering the detector at a small gradient will not pass through the scintillators.

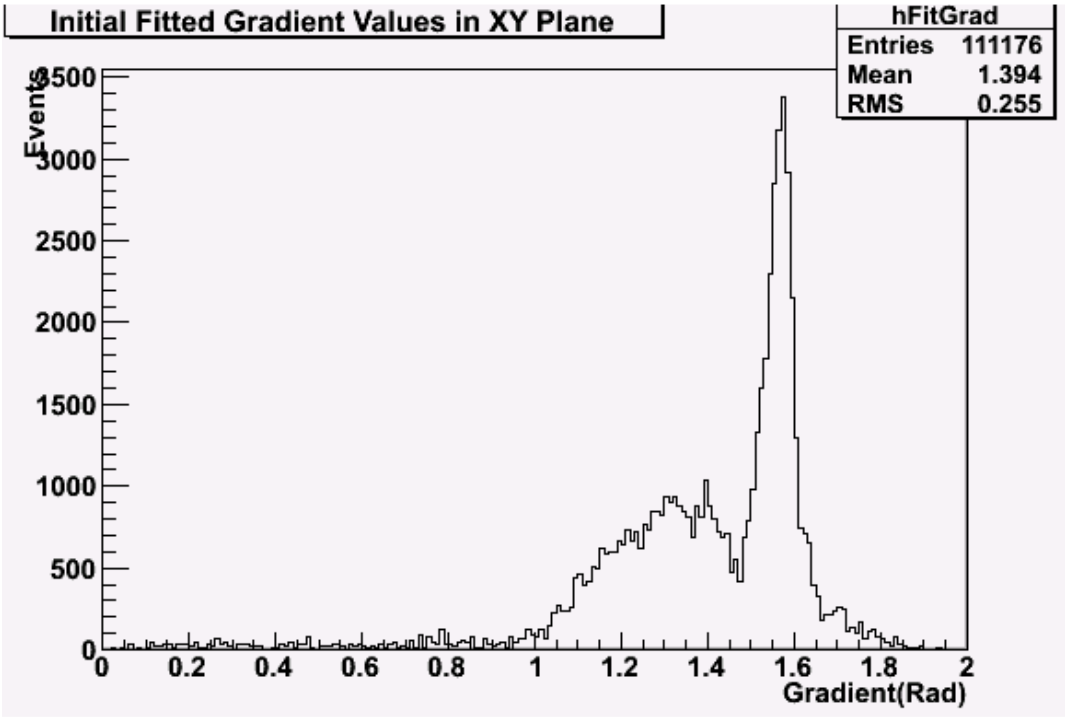


*Figure 4.3: Gradient values in XY plane for threshold T60 data*

Suppose the maximum angle of incidence a cosmic ray could have in order to pass through both scintillators was 45º to the y-axis, then the detectable range of gradient would have been between 0.78 and 2.35 radians. Based on this the few events shown in Figure 4.3 where gradient is outside this range could be attributed to noise events that have been reconstructed.

The peak shown is a feature of the source of cosmic rays [14]. Cosmic rays incident near the vertical will have to pass through less of the Earth's atmosphere and thus more flux will be expected in this direction.

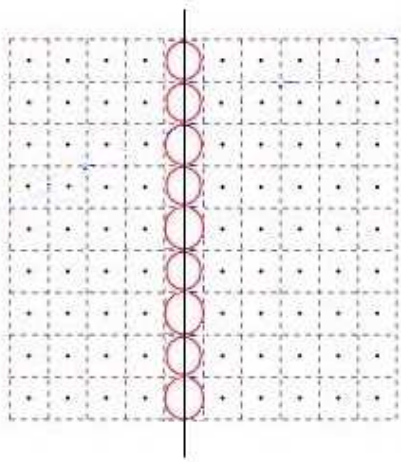

*Figure 4.4: Fit of incident particle close to the vertical*

The sharp peak at π/2 radians is feature of the tracking fit. The tracking programme could not reconstruct paths very accurately when the path of an incident particle is close to the vertical. This is highlighted in Figure 4.4. The cellular automation process will record values close to π/2 radians.

### 4.4 Track Fit Probability

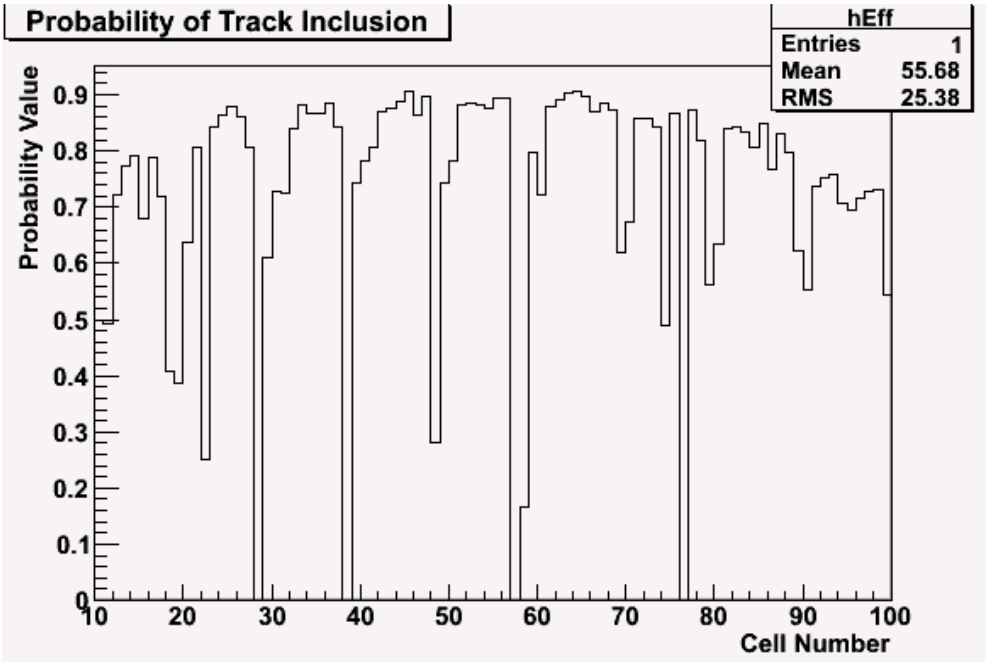


*Figure 4.5: Probability that hit cells will be included in a track fit for the threshold T60*

$P_T$ is the Track fit probability. It is the probability of a hit cell being labelled as a good hit in the track fit. It compares cells that have triggered correctly to noise triggered cells. It is defined as:

$$P_T = \frac{N_G}{N_T}, \tag{16}$$

where $N_G$ is the number of occurrences where a cell is hit and labelled a good hit in the tracking programme and $N_T$ is the total number of times the cell is hit.

Figure 4.5 compares $P_T$ for all 90 cells. Cells 28, 38, 57 and 76 were never involved in the track fit as neither cathode time is recorded. In contrast for hits only recording one cathode time the Z-position can be reconstructed using equation (13). Looking at the shape of the graph, cells in columns 0, 1, 8 and 9 had lower values of $P_T$ due to their position in the 90-Cell. Due to the scintillator trigger position there were more hits in the central columns. It did not affect the probability of the cell being triggered by noise however it is a statistical error on $P_T$ in this instance. If the data were taken for a longer period or another method of triggering was used it would be expected that the $P_T$ distribution would be even.

### 4.5 Threshold Analysis

To investigate the difference between the Geiger card thresholds $D_P$ and $P_T$ were compared over the range 60-A0. The data was taken over a short period with no known changes to the tracker made.

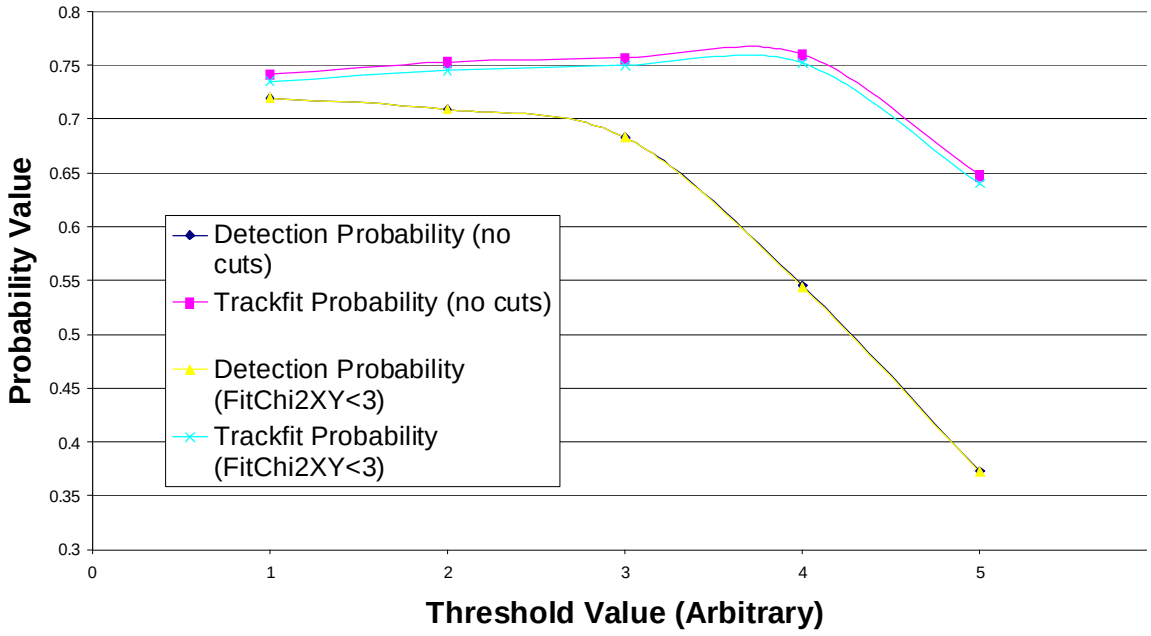


*Figure 4.6: Efficiency value average at various thresholds*

Figure 4.6 displays the results of this. The thresholds were denoted on the x-axis as: T60 = 1, T70 = 2, T80 = 3, T90 = 4 and TA0 = 5. The y-axis shows the average value over the whole 90 cells for the two parameters. It was seen that beyond T70 $D_P$ rapidly decreases and similarly for $P_T$ there was a noticeable decrease beyond T80. This suggested T60 or T70 were the best suited thresholds provided noise events can be discarded efficiently from useful data.

# 5. Data Comparison

## 5.1 T60 & TA0 Comparison

The difference between T60 and TA0 was also investigated to see the affect on the probability of cathode signals passing these thresholds in each cell

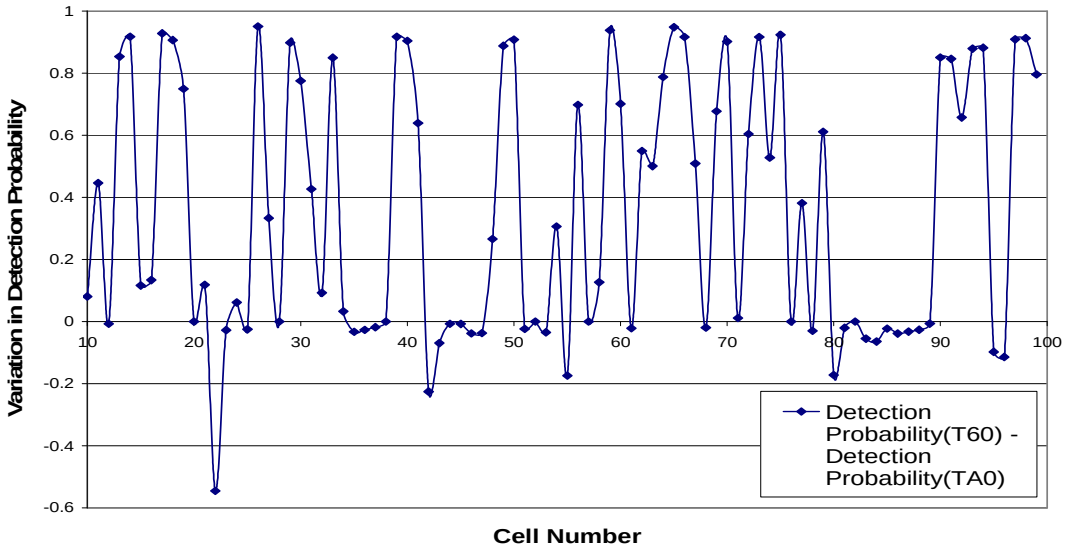


*Figure 5.1: Comparison of detection probabilities in T60 and TA0 threshold*

Figure 5.1 displays the TA0 detection probability data subtracted from the T60 data for all 90 cells. In the majority of cases T60 clearly improved. Many of cells were no change was observed were the cells that were observed to be inefficient in the Geiger card. Accordingly, changes to the threshold did not affect their functionality. However, cells 22, 42, 55, 80, 95 and 96 showed a distinctive loss of propagation efficiency. Cells 95 and 96 are those thought to be inefficient in the cathode as shown in Figure 4.1. This suggests that the inefficiencies in their Geiger cards are different to the other cells with no change in $D_P$ with threshold.

## 5.2 Data from 16th March 2009 and 28th April 2009

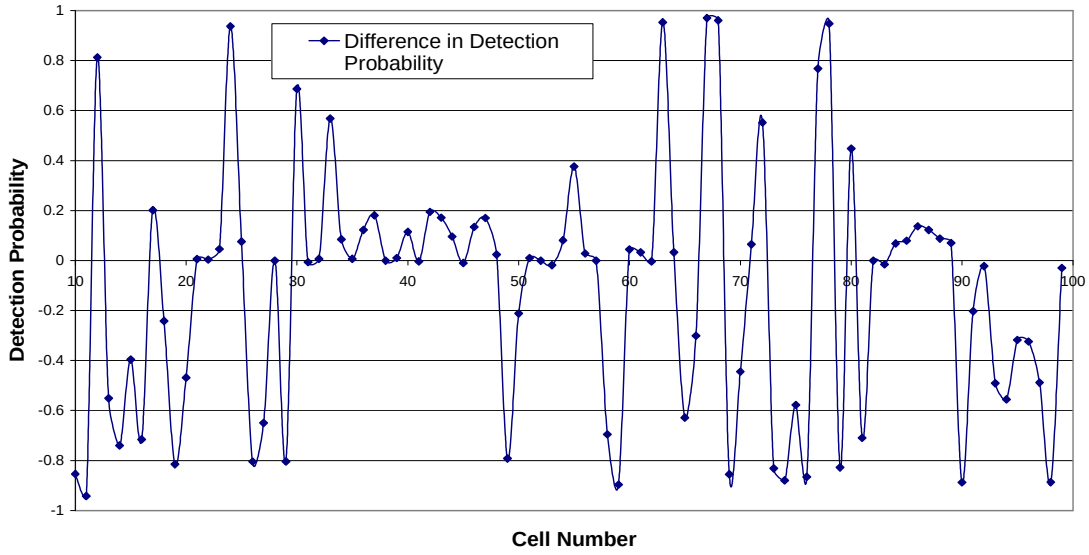


*Figure 5.2: Difference in detection probability between 160309 data and 280409 data*

Fig.5.2 displays the detection probability difference between two sets of data. Data taken on 16th March 2009 is subtracted from data taken on 28th April 2009. Variables in the data sets are the following:

- When disassembling the 90 cell in mid-April many blockages were removed, but a few were seen in new cells.
- A selection of Geiger cards were modified to look for optimum performance after the disassembly.
- The cells in the 16th March 2009 data were powered at 1540V rather than 1550V in the 29th April 2009. These data sets were the closest matched of all available. The voltage difference would explain why a certain proportion of cells seem to increase in detection efficiency by around 10-20%.

Due to the fact some of the Geiger cards have been modified the above data sets are biased. Additionally no previous data existed were the cells were powered at 1550V, before the disassembly data was taken with the cells operating at 1500V. To analyse the differences made to the tracker during the disassembly the same conditions need to be replicated. This has already been seen in single cell analysis were the physical condition of the tracker has improved. Therefore it is concluded that the disassembly has improved the 90-Cell's working condition. This will be seen more clearly once the readout is working fully.

# 6. Studies Propagation Efficiency Relating to Pressure and Temperature

### 6.1 Testing of cell 90

In order to fully account for the pressure and temperature effects, firstly we collected data for the propagation efficiency dependence on voltage for cell 90. It had been determined that through previous tests that this cell was functioning correctly with a relatively high propagation efficiency indicating that it was free from blockages. It would therefore provide a good indicator of how the threshold voltage varied with shifts in barometric pressure. We defined the threshold voltage as the voltage at which the propagation efficiency is equal to 0.5. Data was collected from 12th February 2009 until 3rd March 2009 although additional data was collected between the 8th January 2009 and 19th January 2009 by members of the SuperNEMO group. For the days that we collected data, pressure readings were taken from the standalone barometric pressure sensor in the tracker room. However, for the additional days it was necessary to find the pressure data from an internet source [15]. We assumed that the data would have been collected at about midday, but in general the variation over the working day was small. It was found that this data was in good agreement with the pressure readings that we took. The results of data taken are shown in Figure 6.2.

Data from cell 90 was taken using a device called Combined Analysis and aQuisition (CAQ). It logged the efficiencies of cathode 1 and cathode 2 as well as the total efficiency. The device was controlled using LabVIEW [16] software allowing the voltage value to be inputted from the computer terminal. By using a range of voltages from 1550 V to 1770 V we measured the propagation efficiency on several days.

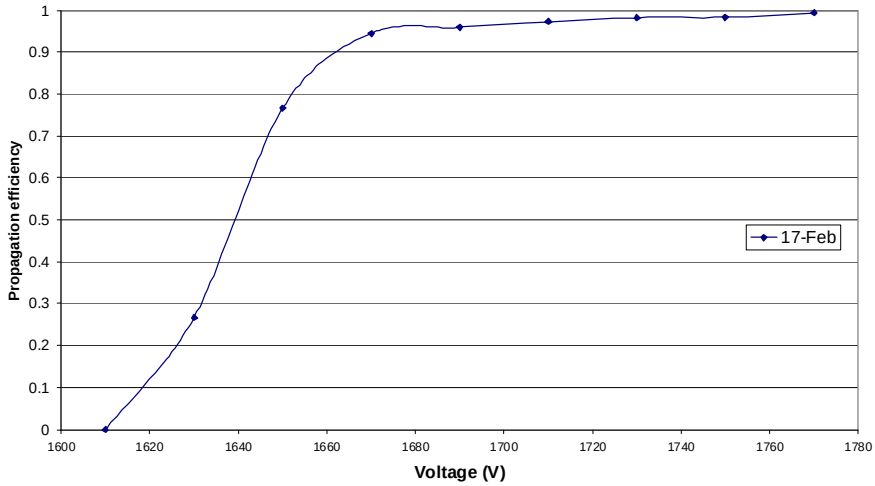


*Figure 6.1: Graph of propagation efficiency and a function of voltage for cell 90 of 17th February 2009*

The shape of the plot shown in Figure 6.1 is fairly typical of the plots of the data collected on the other days. For each data set the threshold voltage was determined using a straight line fit between the voltages that gave propagation efficiencies just above and below 0.5. The relationship between threshold voltage and pressure is shown.

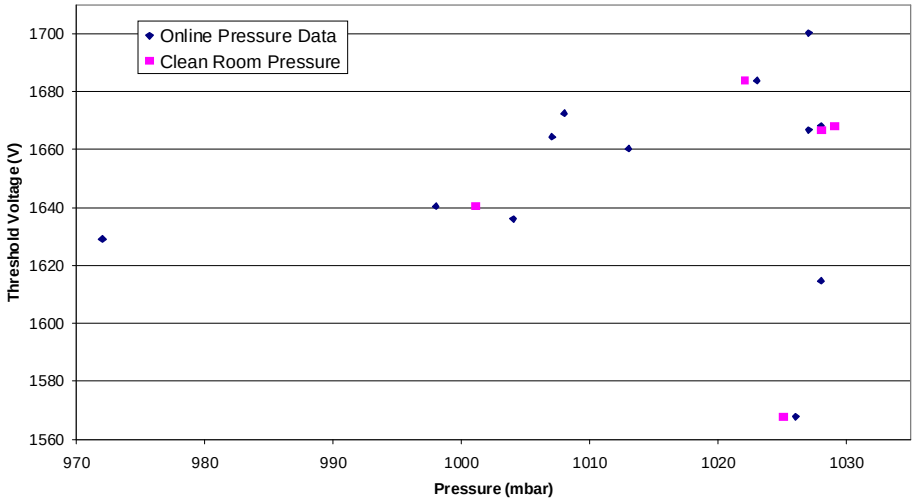


(a)

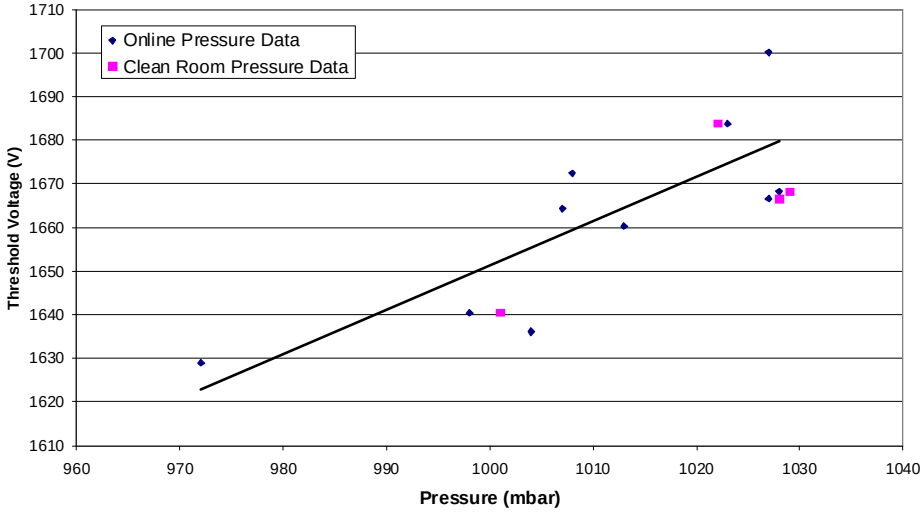


(b)

*Figure6.2: Threshold voltage as a function of pressure (a) with anomalous results (b) without anomalous results*

Figure 6.2 shows a reasonably strong proportional relationship between the threshold voltage and the barometric pressure. After taking some initial measurements on 12th February 2009 it was found that the flow rate of the gas medium had been reduced from 250 ml/minute to 150 ml/minute shortly before this date. The very low threshold values shown on figure 3.2(a) corresponded to this date and it was likely that the low threshold value was related to the decrease in flow rate. A similar anomalous point relates to data collected 8th January 2009 and may be due to a similar reduction in gas flow rate. By removing these points from the plot, as shown in figure 3.2(b), the proportional relationship can be identified more clearly

### 6.2 Development of Pressure and Temperature Logger

After confirming that the shifts in atmospheric pressure were having an effect on the threshold voltage it was decided it was necessary to log the pressure and temperature at regular intervals so that the values could be inputted in to the computer terminal that controlled the voltage output. This would make it possible to write software that could automatically determine if the shift in pressure and temperature would have a significant effect on the effective voltage and if so to adjust the applied voltage to compensate. The data logger that was found to be suitable was called DrDAQ [17]. It could interface with the computer terminal through the printer port and came equipped with a suitable external temperature gauge. The pressure sensor that was used, HCA08811 ARG8 [18], had to be connected to DrDAQ externally. Its voltage output varied in proportion to changes of external pressure. By scaling this detected voltage using a LabVIEW programme it was possible to ascertain a pressure reading. We wrote the programme initially to display the temperature reading and an arbitrary measurement related to the detected voltage from the pressure sensor. The pressure sensor was powered by an external DC voltage source, which when altered caused a shift in the output voltage therefore it was necessary for this voltage source to be stable. To convert the voltage to pressure the proportionality relationship of the pressure sensor between voltage and pressure was used, its gradient being 0.75. Following this a measurement was used to initially calibrate the pressure sensor then readings of pressure $P_m$ could be taken which were given by the relation:

$$P_m = [(V_m - V_0) \times 0.75] + P_0, \tag{17}$$

where $V_m$ is the measured voltage, $V_0$ and $P_0$ are previous measurements of voltage and pressure respectively. $P_0$ was determined from the standalone pressure sensor in the tracker room. The pressure and temperature were logged at five minute intervals overnight to determine the consistency of the collected measurements. The data seemed reasonable since it was collected over a weekend and it was expected that the temperature would decrease slightly and then rise daily. The pressure change was also consistent with the reading taken by the standalone sensor. Figure 6.3 shows similar temperature and pressure data taken on a later run over a sixty-five hour period when the system was in place.

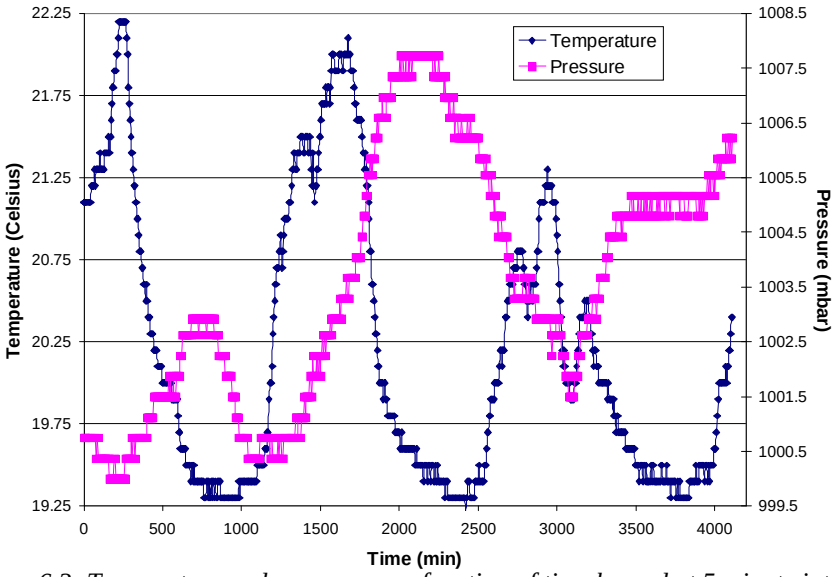


*Figure 6.3: Temperature and pressure as a function of time logged at 5 minute intervals*

## 6.3 Interface with HV Main

Because of the successful testing of the pressure-temperature logger it was decided to interface this detection software programme with the LabVIEW programme that regulated the voltage supply to the tracker called HV Main. This altered the voltage using a device called CAEN. If the relative pressure and temperature term in equation (9) varies then the programme will alter $V_a$ accordingly in order to maintain a constant value of $V_{eff}$. A necessary parameter that was included was that the voltage change would have to be of the order ±3 V before HV Main adjusted it. This was in order to prevent alterations with relatively insignificant changes in pressure and temperature. A data run was performed, as shown in Figure 6.4, displaying the changes in $V_a$. It is the same data run that is shown in Figure 6.3.

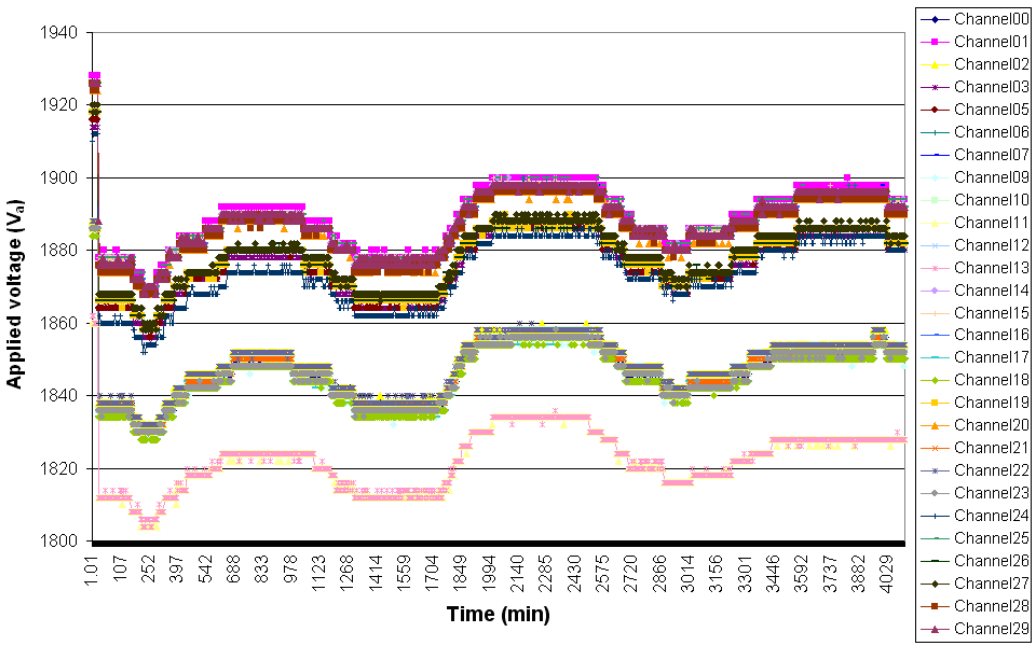


*Figure 6.4: Changes in $V_a$ as a function of time logged at 5 minute intervals*

The CAEN voltage supply is separated into thirty channels. Each supplies a certain number of cells varying from one to six. It should be noted that channel 08 was not being used and hence no data is shown for it. The graph shows that $V_a$ across the tracker ranges from approximately 1800 V to 1900 V. This variation is due the geometry of the cells and their position within the tracker since the electric field on each cell will be affected by those surrounding it. The slight undulation shape of $V_a$ for each channel is the programme compensating for the change in the pressure and temperature as seen in Figure 6.3

A conformation of the success of the system in maintaining a stable value of $V_{eff}$ would be shown in the current on the anode wire of each cell also remaining constant. This is because the current has a proportional relationship to $V_{eff}$. As such we also collected current value data from each channel over the same period that has been discussed. To avoid bias the value for the outputted current was divided by the number of cells that the channel supplied. The results are shown in Figure 6.5.

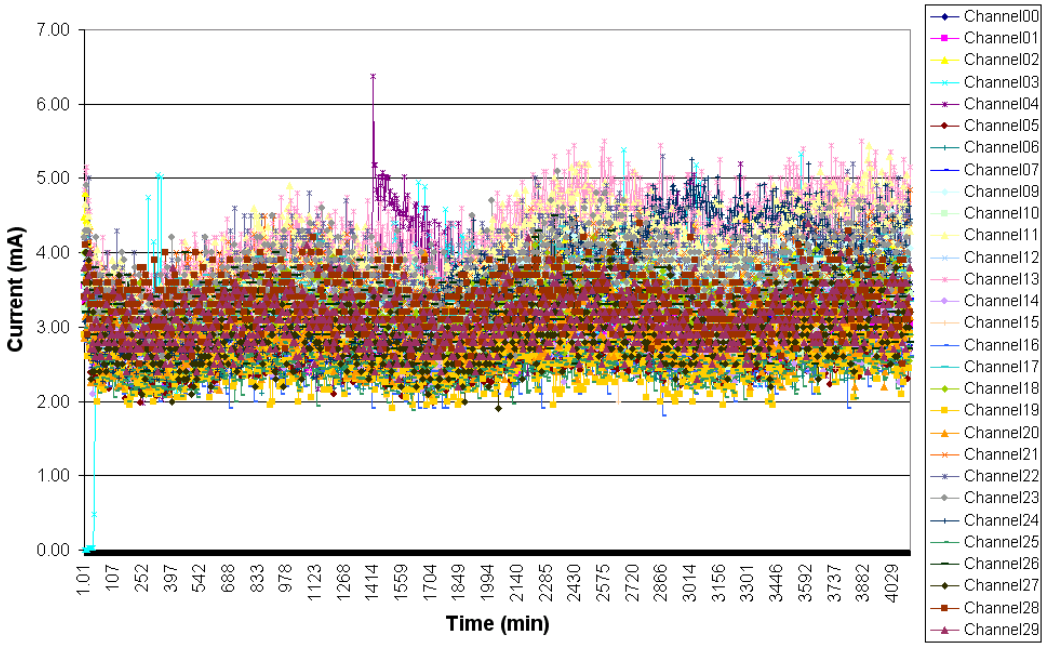


*Figure 6.5: Current per cell as a function of time logged at 5 minute intervals*

It appears that over the time period the current was relatively stable across the majority of the channels. There a several instances where the current was either higher or lower than expected and there is a slight undulation of the current over the period. This effect and the anomalous results are due to factors independent of the DrDAQ system since it has be shown to be working successfully when considering the parameters of its purpose.

## 7. Conclusions

In its current state the 90-Cell has approximately a 25% rate of failure in terms of cathode efficiency, factoring in blockages and readout. However, we have found that the remaining cells function successfully with good propagation efficiency of around 97%. The ultimate objective is to achieve as low a failure rate as possible. Realistically this should be between 1-2%.. The next stage of testing will be to remove the scintillators and use a system of self-triggering whereby the tracker triggers of the first cell that is hit. This will allow for tracking over all angles.

A good analysis of cathode propagation efficiency cannot be done until all Geiger cards are fully operational. This will mean firstly further testing of the Geiger readout needs to be done to calibrate the TDCs and thresholds. Although this report favours the T60 threshold this is based on large cuts of noise events which could be attributed to the lower threshold. There was unexpected behaviour under different thresholds that could be looked at further. For instance in cell 22, $D_P$ was observed to increase with higher thresholds. This could give insight into the changes to be made.

When the 90-Cell was taken apart some supposed physical blockages that had been localised to a certain point on the wire were not found. After cleaning these cells still had low propagation efficiency implying there could be a defect on the surface of the anode wire where the blockage might be. It is recommended to analyse these possible defects under a short wavelength source in order to ascertain whether or not wire defects are responsible.

The current in the 90-Cell was observed to be slightly unstable despite the DrDAQ system regulating a constant $V_{eff}$. It is recommended that further measurements are taken to observe current changes. This will help to gain insight into what external issues are affecting the current stability and determine whether it is possible to normalise these effects so that a constant current can be produced.

## 8. References


[1] R. Arnold et al., Technical design and performance of the NEMO 3 detector, *Nucl. Instrum. Meth.*, A536:79-122, (2005)

[2] K. Eguchi et al., First results from KamLAND: Evidence for reactor and anti-neutrino disappearance, *Phys. Rev. Lett.*, 90:021802, (2003)

[3] H. V. Klapdor-Kleingrothaus, I. V. Krivosheina, A. Dietz, and O. Chkvorets, Search for neutrinoless double beta decay with enriched Ge-76 in Gran Sasso 1990–2003, *Physics Letters B*, 586: 198-216 (2004)

[4] M. G. Inghram and J. H. Reynolds, Double beta-decay of $^{130}$Te, *Phys. Rev.*, 78(6): 822-823, (June 1950)

[5] R. Eisenberg and R. Resnick, *Quantum Physics of Atoms, Molecules, Solids, Nuclei and Particles*, 2nd ed., Wiley and Sons (1985), Chapter 18

[6] T. M. Conneely and T. D. Head, Investigation of Geiger cell prototypes for the SuperNEMO detector, Master's thesis, School of Physics and Astronomy, Manchester, (May 2008)

[7] D. H. Wilkinson, The Geiger discharge revisited. 1. the charge generated. *Nucl. Instrum. Meth.*, A321:195–210, (1992)

[8] J. A. Kadyk. Wire chamber aging. *Nucl. Instrum. Meth*, A300:439, (1991)

[9] M. Alviggi *et al.*, Cosmic ray test station for ATLAS RPC, *Nucl. Instrum. Meth.* A508: 124-174, (2003)

[10] *The 90-cell tracker prototype for SuperNEMO*, University of Manchester, Particle Physics Group (2008)
http://www.hep.manchester.ac.uk/SuperNemo/tracker/90cell/ [Accessed: 16/03/09]

[11] S. Snow, C. Jackson, I. Nasteva, Tracking for the 90-Cell Prototype, *SuperNEMO Collaboration Meeting - Dubna* (2008)

[12] C. Jackson, Status of 90-Cell Tracking, *SuperNEMO Collaboration Meeting – Prague* (2009)

[13] *ROOT*, An Object Orientated Data Analysis Framework, Version 5.20 (2008)

[14] S.Kliewer, *Comparing muon count rates at different altitudes*, SLAC (1995)
Found at:
http://www2.slac.stanford.edu/vvc/cosmicrays/tourstop3.html [Accessed 2/05/09]

[15] *Weather Underground*, Weather Underground Inc. (2009)
Found at:
http://www.wunderground.com [Accessed 12/02/2009]

[16] *LabVIEW*, National Instruments Inc., Version 8.5 (2007)

[17] *DrDAQ Data Logger*, Pico Technology Ltd. (2007)
Full specification found at:
http://www.picotech.com

[18] *HCA-BARO Series: Miniature amplified barometric pressure sensor*, Sensortechnics (2008)
Full specification found at:
http://www.sensortechnics.com